nature communications

Article https://doi.org/10.1038/s41467-023-37154-z

Substantial lifetime enhancement for Si-based photoanodes enabled by amorphous TiO_2 coating with improved stoichiometry

Received: 18 October 2022

Accepted: 3 March 2023

Published online: 04 April 2023

Check for updates

Yutao Dong[1], Mehrdad Abbasi[2], Jun Meng[1], Lazarus German[1], Corey Carlos[1], Jun Li[1], Ziyi Zhang[1], Dane Morgan[1], Jinwoo Hwang[2] & Xudong Wang[1]

Amorphous titanium dioxide (TiO_2) film coating by atomic layer deposition (ALD) is a promising strategy to extend the photoelectrode lifetime to meet the industrial standard for solar fuel generation. To realize this promise, the essential structure-property relationship that dictates the protection lifetime needs to be uncovered. In this work, we reveal that in addition to the imbedded crystalline phase, the presence of residual chlorine (Cl) ligands is detrimental to the silicon (Si) photoanode lifetime. We further demonstrate that post-ALD in-situ water treatment can effectively decouple the ALD reaction completeness from crystallization. The as-processed TiO_2 film has a much lower residual Cl concentration and thus an improved film stoichiometry, while its uniform amorphous phase is well preserved. As a result, the protected Si photoanode exhibits a substantially improved lifetime to ~600 h at a photocurrent density of more than 30 mA/cm^2. This study demonstrates a significant advancement toward sustainable hydrogen generation.

Photoelectrochemical (PEC) water splitting is considered a promising sustainable energy path to hydrogen fuel generation[1]. Silicon (Si) is a commonly used photoanode material that is expected to deliver the highest energy conversion efficiency owing to its appropriate band structure and excellent charge mobility[2,3]. However, Si also exhibits a very short lifetime of only a few hours, as it would experience rapid corrosion or dissolution in alkaline electrolytes[4]. To improve its lifetime, a prevailing strategy is to protect the reactive photoanode surfaces with a conformal and pinhole-free inert oxide coating by atomic layer deposition (ALD)[5–7]. While both crystalline and amorphous ALD oxide films have been applied for surface protection[8], amorphous coating are more commonly used owing to its excellent uniformity and conformality. The highest reported lifetime of Si-based photoanode was achieved by amorphous TiO_2 coating at the level of 500 h[2,6,8–12], which, however, is still far from the minimal industrial requirement (30,000 h)[13]. Further improving the lifetime appeared to be stunted. A wide variety of performances have been reported from ALD coatings from different growth systems or slightly changed deposition conditions[9,11,14,15], limiting the reproducibility and scaling up of this promising strategy in energy applications. Other ALD oxide films, such as Al_2O_3, HfO_2, and ZrO_2, have also been explored as a protective coating. Their protection performances were generally lower than TiO_2, possibly due to their lower conductivity and structural uniformity[10,16,17].

Despite the broad use of ALD for surface protection, the essential structure-property relationship that dictates the protection lifetime control is still largely missing. Typically, the amorphous ALD films are considered homogeneous. Their protection performances are primarily tuned by thickness and deposition temperature. Among the limited understandings of the protection lifetime control, a few reports correlated the protection failure with extrinsic impurities or nanoparticles[14,15,18–20]. They revealed that failure typically starts from pinhole formation, which is consistent across different electrode systems. However, current studies still cannot fully answer the fundamental question, i.e., what is the correlation between ALD process, structure, and chemistry of the amorphous films, and their chemical and physical properties, which determines the protection performance? This knowledge gap places the main hindrance to further improving the PEC electrode lifetime to meet the industrial standard. Our previous study

[1]Department of Materials Science and Engineering, University of Wisconsin-Madison, Madison, WI 53706, USA. [2]Department of Materials Science and Engineering, The Ohio State University, Columbus, OH 43210, USA. e-mail: xudong.wang@wisc.edu

revealed that structural inhomogeneity in the amorphous film (e.g., imbedded intermediate phases) could induce a highly localized current through the amorphous film and facilitate pinhole formation[9]. While this study suggested a low-temperature crystalline-free amorphous film is preferable for achieving a long lifetime, the unreacted precursor ligands and byproducts were another inevitable issues associated with the low-temperature ALD processes. These impurities could substantially change the film properties, such as electronic and ionic transport properties, mechanical stability, and chemical reactivity[21–24], which may open another pathway to breaking the current protection lifetime limit. In this paper, we report a fundamental discovery of the detrimental role of the residual Cl ligand in amorphous TiO_2 films to the PEC protection lifetime. We further developed a post-ALD in situ water treatment procedure. It was able to partially remove the Cl residues and improve the film stoichiometry without introducing any additional crystallization. The processed amorphous TiO_2 film showed drastically improved chemical stability, and thereby substantially elongated the lifetime of Si photoanodes to ~600 h in an alkaline electrolyte. The result will bring direct impacts to the next-generation solar fuel production devices with enhanced lifetime and stability.

Results

Failure of Amorphous ALD TiO_2 coating in PEC protection

The typical configuration of a Si-based photoanode is illustrated in Fig. 1a. The surface of the n-type Si photoabsorber was coated by an ultrathin film of amorphous TiO_2 via ALD, followed by a layer of Ni acting as the oxygen evolution reaction (OER) catalyst. The conformal amorphous TiO_2 coating prohibits OH^- group diffusion thus protects the Si surface from chemical corrosion. The ALD TiO_2 layer can also passivate Si surface defect states to suppress charge recombination at the interface[25]. Meanwhile, the ultrathin film still permits adequate hole transport through defect band conduction, allowing for unimpaired PEC efficiency[11,26]. Owing to the excellent conformality of ALD, the as-deposited TiO_2 showed an extremely clear and smooth surface without any observable particle features (Fig. 1b). Atomic force microscopy (AFM) topography scan revealed that the average surface roughness of TiO_2 was only 0.33 nm, confirming the outstanding smoothness and uniformity (Fig. 1c). The structure of as-deposited TiO_2 films were examined by scanning transmission electron microscopy (STEM). Figure 1d shows the cross-section of a 15-nm-thick TiO_2 film on Si, which was free of any particles. The nano-diffraction pattern of the TiO_2 film indicated a completely amorphous phase without any crystalline phases (Inset of Fig. 1d)[9]. X-ray photoelectron spectroscopy (XPS) survey spectrum showed strong Ti and O peaks confirming the film's chemical composition (Fig. 1e). In addition, an appreciable Cl signal was also detected. The existence of Cl elements could be attributed to the unreacted Cl ligand from the $TiCl_4$ precursor at a relatively low deposition temperature (100 °C)[27].

The high homogeneity of the amorphous TiO_2 film without any observable crystalline phases is a desired coating feature that is

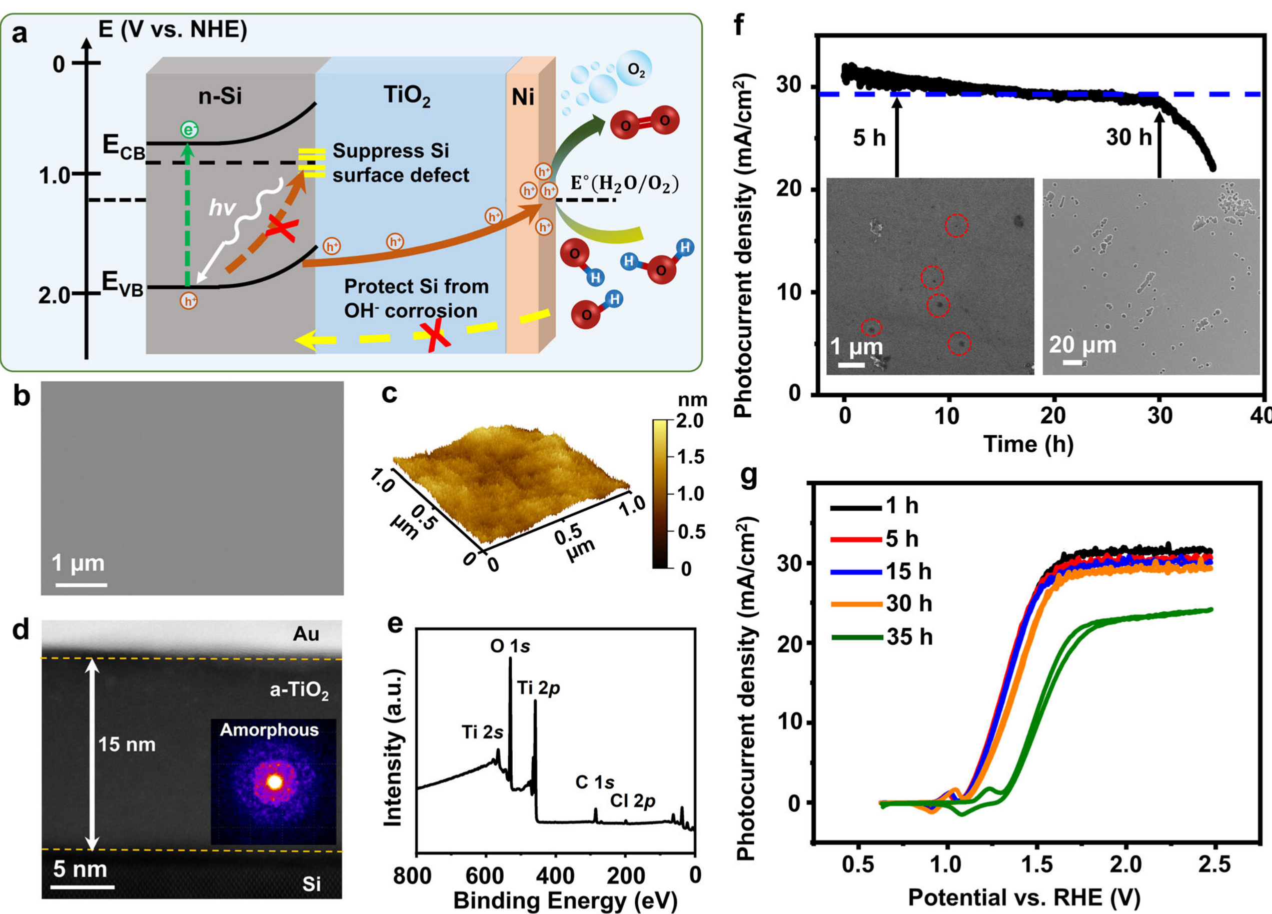

Fig. 1 | Si photoanodes protected by amorphous TiO_2 thin film coating. **a** Schematics of a Si/TiO_2/Ni photoanode for PEC water oxidation. The relevant electronic energy levels in different materials are schematically shown. NHE normal hydrogen electrode, CB conduction band, VB valence band. **b** SEM image of as-deposited amorphous TiO_2 thin film on n-Si substrate. **c** AFM topography of the TiO_2 surface. **d** Cross-sectional STEM image of Si/TiO_2. Inset is a nano-diffraction pattern taken from the TiO_2 region. **e** XPS survey spectrum of the TiO_2 film on Si wafer. **f** Chronoamperometry test of Si/TiO_2/Ni photoanode measured in 1.0 M KOH aqueous solution under 1 sun illumination at an external bias of 1.8 V vs. RHE. The blue line marks 90% of the original J_{ph} value. Insets show Si/TiO_2/Ni surfaces after 5 h (left) and 30 h (right) chronoamperometry test. **g** J_{ph}-V curves of Si/TiO_2/Ni photoanode obtained at a series of time points from the chronoamperometry test.

expected to bring high stability and a long lifetime to the Si-based PEC system in alkaline electrolyte[8,9]. To reveal the protection performance of this homogeneous amorphous TiO_2 thin film, the complete n-Si/TiO_2/Ni photoanode was placed in a 1 M KOH aqueous solution under 1 sun illumination for PEC water oxidation tests. It should be noted that the sputtered Ni catalyst film remained flat and did not introduce any damage to the TiO_2 surface (Figs. S1, S2). They were electrochemically converted to $Ni(OH)_2$ sheet-like structure during the PEC test (Fig. S3). The PEC performance was investigated in a three-electrode system. Chronoamperometry test at a bias of 1.8 V versus reversible hydrogen electrode (RHE) revealed a quick photocurrent density (J_{ph}) decay (Fig. 1f), where the original value dropped by 10% within just 30 h. At the point of failure (defined as the time point when J_{ph} reached <90% of its original value), a large number of interconnected pores appeared on the electrode surface (right inset of Fig. 1f and Fig. S4a), suggesting low stability of this TiO_2 coating. These pores were evolved from small pinholes as early as a few hours of operation, while J_{ph} was still >95% of its original value (Left inset of Fig. 1f and Fig. S4b). The large pores would isolate the Si photoabsorber from the Ni catalyst layer, and facilitate the formation of insulating SiO_x that limits the hole transport from Si to Ni catalyst. As a result, the Si/TiO_2/Ni photoanode PEC performance was impaired. The J_{ph} vs. potential (V) curves were recorded at a few time points through the chronoamperometry test (Fig. 1g). In the first hour, the water oxidation onset potential was 1.08 V versus RHE and J_{ph} reached a saturated value of 31.5 mA/cm^2 at 1.8 V versus RHE. The saturated J_{ph} and onset potential were on par with reported benchmark n-Si-based photoanodes[11,16,28–30], indicating the high quality of our Si/TiO_2/Ni system. This onset potential was kept steady for the first 15 h, but quickly shifted positively to 1.11 and 1.24 V versus RHE at the 30-h and 35-h operation time points, respectively (Fig. 1g). The higher onset potential implied the increase of charge transfer resistance in the PEC system, which is typically induced by the formation of insulating SiO_2 layer due to Si corrosion[31,32]. Accordingly, saturated J_{ph} dropped continuously to 30.2, 29.8, 28.8, and 21.9 mA/cm^2 at the PEC operation time of 5, 15, 30, and 35 h, respectively, consistent with the decay trend in the stability test. During PEC operation, because no extra redox peaks other than the $Ni(OH)_2$/NiOOH couple were observed from the J_{ph}-V curves, it can be hypothesized that the corrosion of the TiO_2 layer was a result of chemical dissolution without valence change.

To test this hypothesis, the TiO_2-coated Si wafer was immersed into a 1 M KOH aqueous solution to evaluate the chemical stability of the amorphous TiO_2 film. Without an external bias, the TiO_2-coated Si wafer still exhibited obvious corrosion but with square-like pores, a typical morphology of chemically corroded Si wafer in an alkaline solution (Fig. S5)[18,33]. This type of corrosion was also started from pinholes (Fig. S5a–c) as a result of TiO_2 dissolution confirmed by XPS analyses (Fig. S6a–c), suggesting the chemical reactivity of as-deposited TiO_2 would primarily be responsible for the failure. Considering the presence of an appreciable amount of precursor ligand residues (Cl from $TiCl_4$ precursor, Fig. 1e) in the film, the unreacted Cl ligands acted as the terminating point in the Ti-O-Ti network, and thus could introduce a more permeable amorphous lattice allowing fast reaction between OH^- and Ti-O[34]. In addition, DFT calculation revealed that residual Cl ligands could also induce in-gap defect states at the middle of the band gap and shifted the Fermi level from 2.71 eV (Fig. 2a) to 4.14 eV (Fig. 2b) closer to the conduction band, which can enhance the hole conductivity of the amorphous TiO_2 film[12,26]. This localized conductivity increase is able to induce local OH^- accumulation at the electrode surface, which facilitates the reaction between OH^- and TiO_2[9]. Together, in the PEC system, Cl residues could enable a faster dissolution of TiO_2 and a rapid diffusion of OH^- to reach the vulnerable Si surface (Fig. 2c)[35–37].

Water-treated amorphous TiO_2 with improved stoichiometry

Due to the destructive residual Cl ligands, therefore, it is intuitive to hypothesize that a longer protection lifetime may be achieved by reducing the residual Cl ligands in amorphous TiO_2 film. Meanwhile, no crystallization should be induced, as crystalline phases can introduce structural inhomogeneity and jeopardize the film's lifetime. To achieve this goal, a post-ALD water treatment procedure is developed to reduce the residual Cl ligands and maintain amorphous film homogeneity simultaneously. As schematically illustrated in Fig. 3a, after the regular TiO_2 ALD cycles are completed, the sample was kept in the growth chamber subjecting to additional 2400 water pulses under the same temperature and vacuum. During this treatment, water molecules could diffuse into the amorphous TiO_2 matrix and react with the dangling Cl ligands, which raises the film's stoichiometry and improves the Ti-O-Ti network continuity. This post-ALD water treatment could well preserve the surface flatness and conformality of the as-deposited TiO_2 film. No additional nanoparticles were observed from the film surface (Fig. 3b). AFM topography scan revealed that the TiO_2 surface kept the same extremely low roughness of ~0.3 nm (Fig. 3c). XPS Cl $2p$ spectra showed an apparent intensity drop of both Cl $2p_{3/2}$ (198.16 eV) and Cl $2p_{1/2}$ (199.82 eV) peaks (corresponding to the Cl-Ti bonding[27,38]) after water treatment (Fig. 3d). The fine Ti $2p$ spectra of both pristine and water-treated films showed an almost identical shape with the dominating Ti^{4+} chemical state located at 459 eV (Fig. 3e), implying the water treatment did not change the chemical state of Ti^{4+} cation in the network. By integrating the Cl, O, and Ti peaks areas as a half-quantitative analysis, the Cl:Ti ratio was found reduced by 27% (from 0.062 to 0.045), confirming a substantial removal of residual Cl ligands from the amorphous TiO_2 film.

Four-dimensional scanning electron microscopy (4D-STEM) based characterizations were further used to confirm the elemental and structural change from water treatment. The presence of two blurry rings in the averaged nano diffraction patterns revealed that no additional crystallization was induced by the water treatment (Fig. 4b) as compared to the pristine TiO_2 film (Fig. 4a). Diffraction also suggested the existence of the medium-range ordering (MRO) in both TiO_2 amorphous films. MRO refers to the nanoscale volumes with relatively high structural ordering within amorphous materials[39]. Here, the variance (V) of the nano diffraction intensity as a function of reciprocal lattice vector k, $V(k)$ was used to measure the degree of MRO (Fig. 4c). The magnitude of the peak is related to the degree of structural fluctuation created by the distribution of MRO domains, and the peak position is related to the type of MRO. The broad peak at ~3.0 nm^{-1} indicates the MRO was substantially disordered, confirming the amorphous phase. After water treatment, the broad peak position was retained without shifting, demonstrating disordered MRO structure was well maintained. The slightly increased peak intensity may be related to Cl ligands removal. The change of Cl distribution was directly visualized using long-time energy dispersive spectroscopy (EDS) Cl mapping acquired from the cross-section of both TiO_2 film samples. Compared to the uniform distribution of the Cl signal in the pristine TiO_2 film (Fig. 4d), the Cl signal in the water-treated TiO_2 film was clearly decreased with a concentration gradient, where the Cl signal was nearly undetectable from the top ~5 nm region. EDS spectrums were then collected from the top and bottom regions (marked by red dashed boxes) to quantify the location-dependent chemical composition change (all peak intensities were normalized by the Ti K peaks for comparison). Comparing the water-treated TiO_2 film (Fig. 4f) to the pristine TiO_2 film (Fig. 4e), Cl:Ti ratio in the bottom region was reduced from 3.86 to 2.41% and in the top region was reduced from 2.46 to 1.81%. These characterizations further confirmed that post-ALD water treatment was able to partially remove residual Cl ligands without introducing additional crystallization to the amorphous ALD TiO_2 films.

https://doi.org/10.1038/s41467-023-37154-z

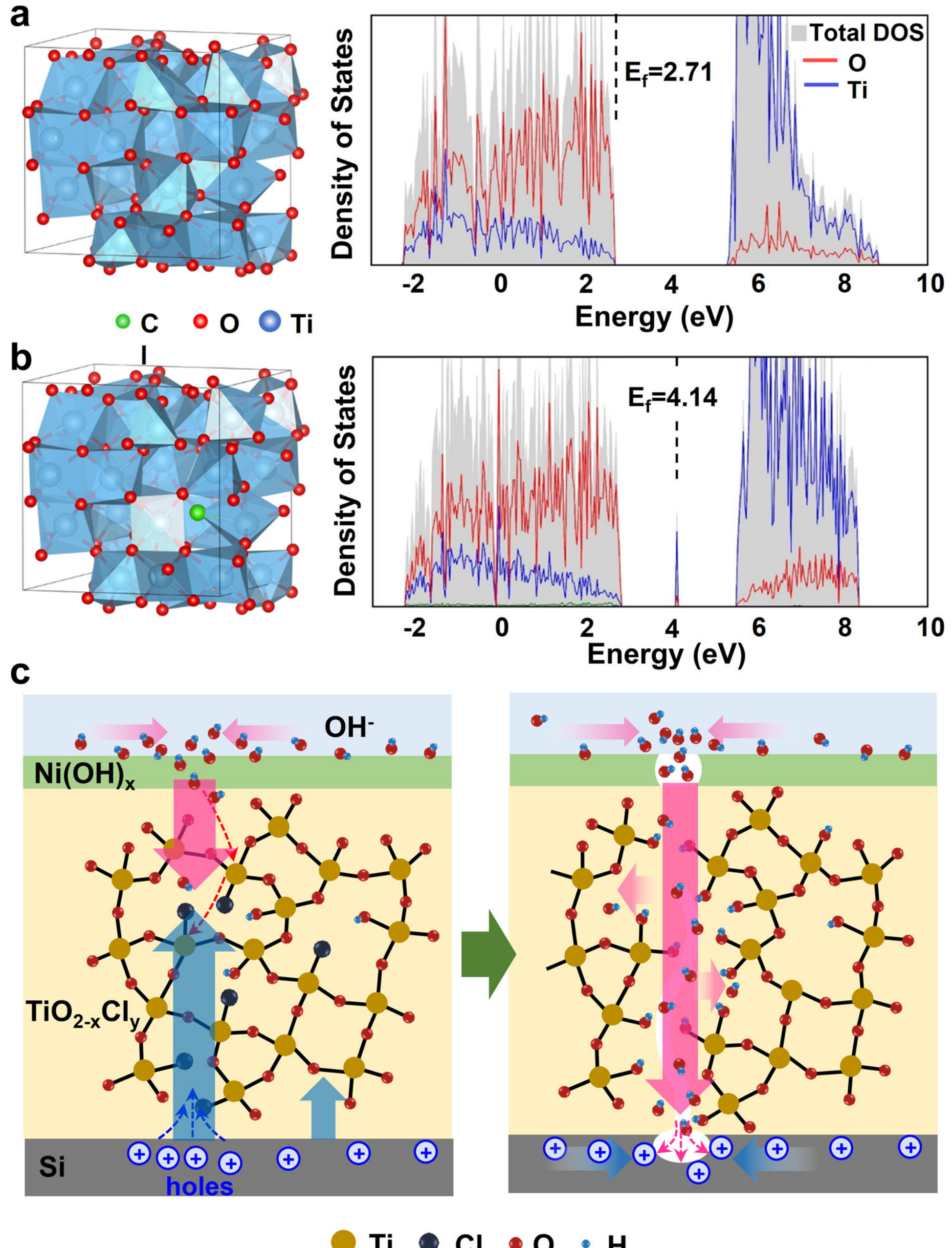

Fig. 2 | Cl-related TiO_2 failure mechanism. **a**, **b** Density of states of the melt-quenched amorphous TiO_2 and $TiO_{1.965}Cl_{0.035}$ models calculated by DFT. The left insets are the polyhedral visualization of the structure of amorphous TiO_2 and $TiO_{1.965}Cl_{0.035}$. **c** Schematics of a possible mechanism of pinhole formation in Cl-containing amorphous TiO_2 films during PEC water oxidation.

PEC stability by water-treated amorphous TiO_2 coating

The chemical stability of water-treated TiO_2 films was then evaluated by immersing the treated Si/TiO_2 sample in a 1 M KOH aqueous solution without applying any external bias. Compared to pristine TiO_2-coated Si, the density of square-like corrosion spots were substantially reduced from ~300 to ~30 mm^{-2}, with smaller spot sizes (Fig. S5). XPS elemental analysis revealed nearly identical Cl 2*p*, Ti 2*p*, and O 1*s* peak intensities after immersion (Fig. S6d–f), indicating that the TiO_2 film after water treatment could be largely preserved when facing an alkaline solution. Electrochemical impedance spectroscopy (EIS) of Si/TiO_2 electrodes was applied to study the possible TiO_2 film conductivity change induced by Cl removal (Fig. 5a). The Nyquist plots were fitted based on the equivalent circuit model (Inset of Fig. 5a). The Si/TiO_2 electrodes with and without water treatment showed similar charge transfer resistance at the high-frequency region, suggesting partially removing Cl did not impair the charge transport property of the TiO_2 film.

Above characterizations confirmed that post-ALD water treatment was able to largely improve the chemical stability and preserve good electrical conductivity. To further evaluate its influences on the PEC performance, the same amount of Ni catalysts was deposited on Si/TiO_2 for water oxidation reaction under the same conditions. Figure 5b compares the J_{ph}-V curves of Si/TiO_2/Ni photoanodes with and without water treatment. Both curves exhibited similar onset potential and saturated J_{ph}. The slightly increased slope of the J_{ph}-V curve from the water-treated TiO_2 sample suggests there might be less amount of charge recombination due to the improved charge transport property[40]. With the improved PEC performance, the

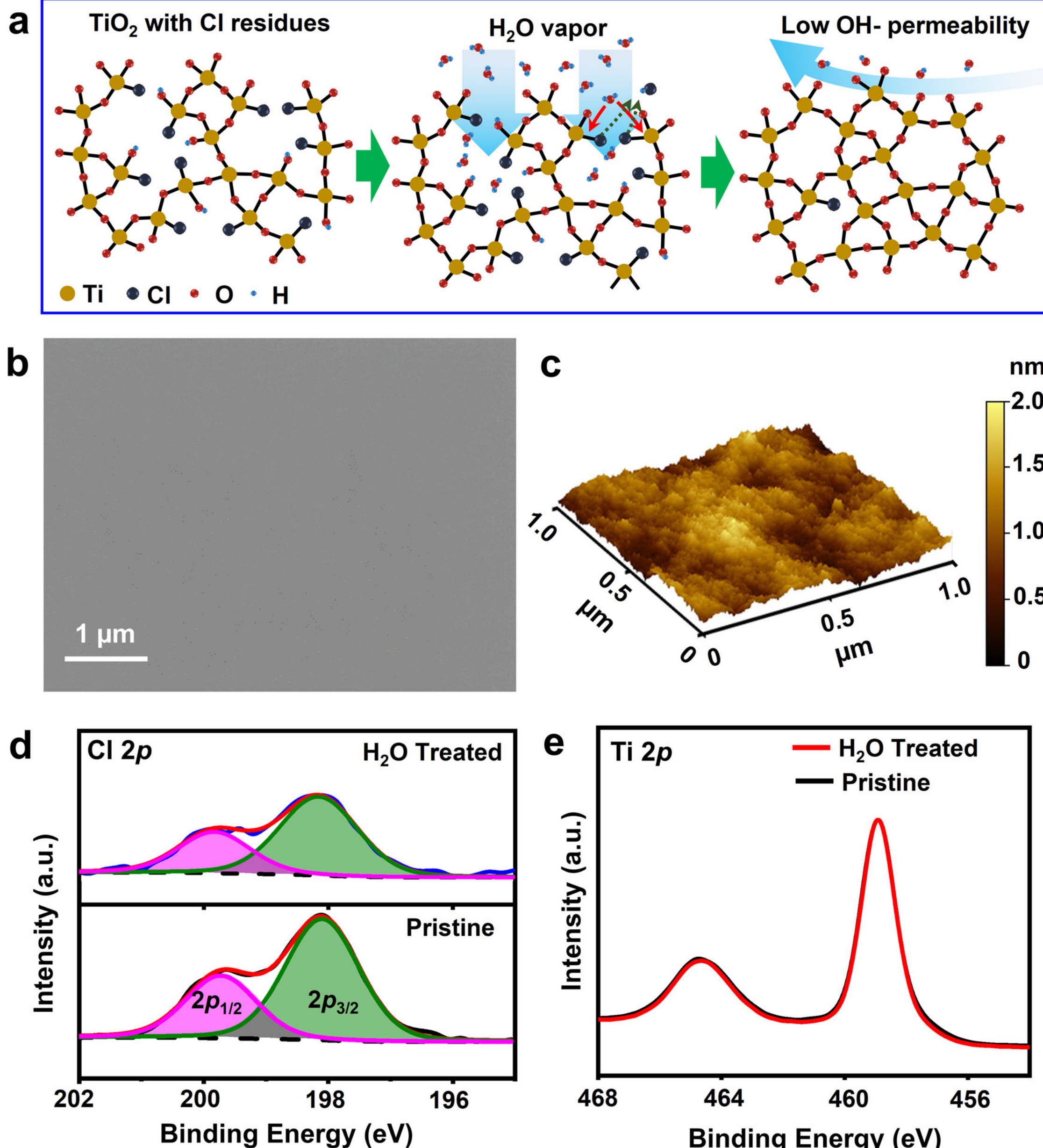

Fig. 3 | Water treatment of amorphous TiO_2 films. a Schematics of water treatment showing the unreacted Cl ligands in amorphous TiO_2 (Left) being removed by reacting with H_2O molecules diffused through the film surface (center) and forming a more continuous, interconnected Ti-O-Ti network. **b** SEM image of the amorphous TiO_2 film after being treated under pulsed water vapor exposure. **c** AFM topography of the water-treated TiO_2 surface with nearly the same surface roughness as the pristine films. **d**, **e** XPS core spectra of Cl 2*p* (**d** red and green area are integrated Cl $2p_{1/2}$ and $2p_{3/2}$ peak. Black dash lines are baselines for peak area integration.) and Ti 2*p* (**e**) comparison between pristine and water-treated TiO_2 thin films.

chronoamperometry test was conducted at an external bias of 1.8 V versus RHE. A stable J_{ph} at ~30 mA/cm^2 was recorded for up to ~600 h (Fig. 5c), about one order of magnitude longer than the pristine TiO_2-protected Si photoanodes. J_{ph}-V curves were also recorded at a series of reaction time points to understand the PEC property change during this long operation period (Fig. 5d). The J_{ph}-V curve maintained an identical shape for the first >100 h, where the electrode surface was nearly intact showing extremely high stability (Fig. 5e-i). The slope started to show a subtle decrease till ~250 h. By that time, only a few small pinholes were evolved on the electrode surface (Fig. 5e-ii). As the reaction time extended, the $Ni(OH)_2$/Ni(OOH) redox peaks and the saturated potential gradually shifted anodically, and the J_{ph}-V curve slope slightly decreased. Both can be attributed to the increase of charge transfer resistance due to the formation of SiO_x on the Si surface. The saturated J_{ph} was almost maintained at the same ~30 mA/cm^2 throughout the entire testing period, evidencing the long-term high water oxidation performance. Owing to the much higher chemical stability of the water-treated TiO_2 films, the evolution from several pinholes to large interconnected pores was substantially suppressed. Therefore, the Si photoabsorber and the TiO_2/Ni catalyst layer could still maintain a tight connection and allow nearly impaired charge flow before the formation of large pores. When the photoanode approached its failure point at 600 h, the J_{ph}-V curve exhibited a drastic anodic shift and the saturated photocurrent density decreased apparently. At this point, large and interconnected pores would be observed on the electrode surface (Fig. 5e-iii), indicating the water-treated TiO_2 film may still share the same failure mechanism as the pristine TiO_2 films.

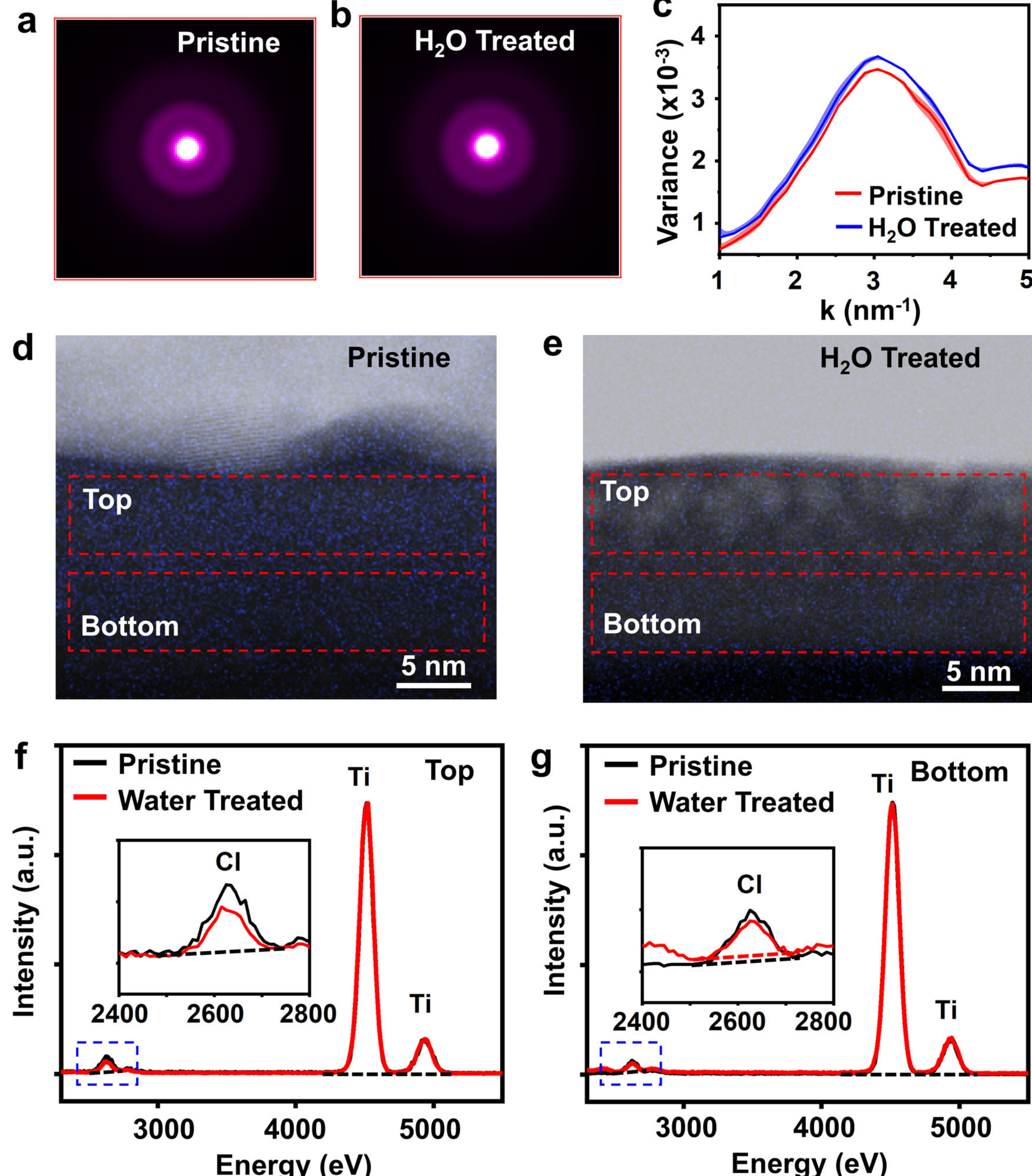

Fig. 4 | 4D-STEM characterization and comparison of pristine and water-treated TiO_2 films. **a**, **b** Averaged 4D-STEM nano-diffractions of pristine (**a**) and water-treated (**b**) TiO_2 film, showing both films had a pure amorphous phase without any crystalline impurities. **c** Comparison of the experimental $V(k)$ between pristine (red) and water-treated (blue) TiO_2 films. Shade areas represent the uncertainty range of $V(k)$. **d**, **e** Cross-sectional EDS Cl mapping of pristine and water-treated TiO_2 films supported on Si wafers. Red dash boxes defined the top and bottom regions in the cross sections, where EDS signals were collected. **f**, **g** EDS spectra of pristine and water-treated TiO_2 collected from the top (**f**) and bottom (**g**) regions from the cross sections. (peaks were normalized by the Ti K peaks). Insets are enlarged Cl peaks in the blue dash box to show the intensity change after water treatment. Black dash lines are baselines for peak area integration.

Discussion

From the above studies, the excellent PEC stability could be attributed to the reduced Cl concentration and improved film stoichiometry without introducing an additional crystalline phase in the amorphous TiO_2 coating, a key structural feature enabled by the post-ALD water treatment. This was because when the ALD growth was completed, the 3D amorphous TiO_2 matrix was formed, and the completely coordinated Ti-O largely restricted their diffusion to form an ordered TiO_2 crystal lattice. It is important to point out that this post-ALD water treatment is fundamentally different from other regular approaches to improve the stoichiometry of ALD films. Reducing the residual ligands (i.e., raising the ALD reaction completeness to improve the stoichiometry) and suppressing the crystallization are always coupled and anticorrelated in regular ALD processes. For example, extending the length of the ALD water pulse can improve the reaction completeness per cycle. However, the extended reaction time could also facilitate surface diffusion of as-deposited species that were loosely bonded to the surface. This may enable the rearrangement of surface atoms and form local nuclei on the surface[41–44], which could serve as seeds for TiO_2 to grow into nanoparticles. As shown in Fig. S7, after elongating the water pulse time from 0.5 to 6.5 s, Cl $2p$ core spectrum showed an apparent peak intensity drop, validating the improved ALD reaction

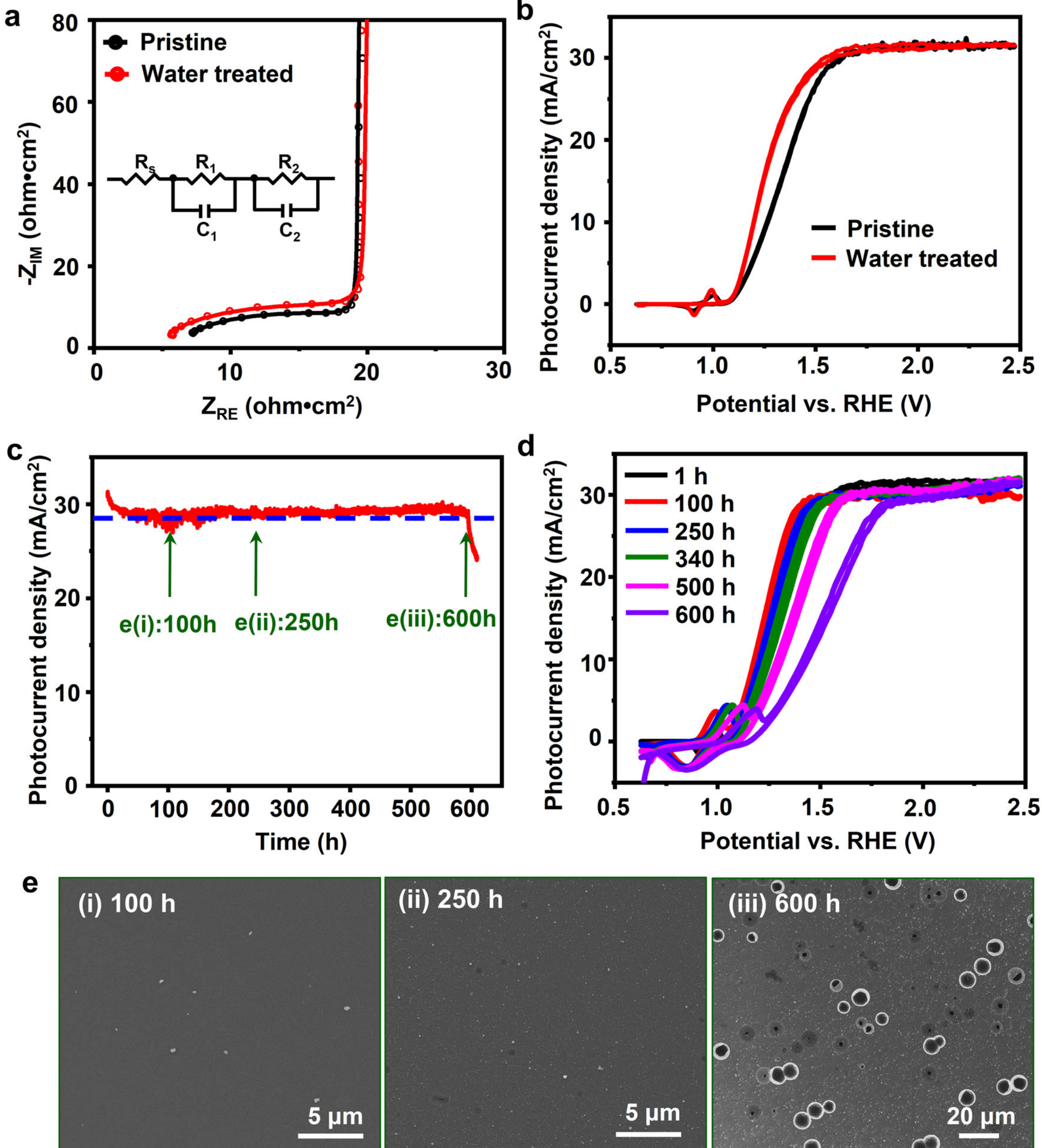

Fig. 5 | Lifetime evaluation of water-treated TiO_2 film for Si photoanodes protection. a EIS measurement of photoanodes protected by pristine and water-treated TiO_2 films under 1 sun illumination. Inset is the equivalent circuit for curve fitting. **b** J_{ph}-V curves of Si/TiO_2/Ni photoanodes protected by pristine (black) and water-treated (red) amorphous TiO_2 films. **c** Chronoamperometry of the Si/TiO_2/Ni electrode (with water treatment) measured in 1.0 M KOH aqueous solution under 1 sun illumination at an external bias of 1.8 V vs. RHE. The blue line marks 90% of the original J_{ph} value. **d** J_{ph}-V curves of Si/TiO_2/Ni photoanode (with water treatment) obtained at a series of time points from the chronoamperometry test. **e** SEM images of the photoelectrode surfaces collected at 100 h (i), 250 h (ii), and 600 h (iii) during the chronoamperometry test, revealing the very slow surface corrosion.

completeness. However, the as-prepared TiO_2 film exhibited a large number of nanoparticles on the surface and the corresponding structure heterogeneity would yield an impaired protection performance (Fig. S8a, b). Similarly, due to the lower energy barrier for nucleating, particularly the intermediate phases of TiO_2 at the active growth surfaces[9], other regular approaches to achieving complete ALD reactions, such as raising the temperature or introducing plasma, are always associated with undesirable crystallization, which also jeopardizes the protection lifetime as earlier research discovered[38,45]. For example, TiO_2 film deposited under 160 °C yielded a large number of crystalline nanoparticles in the amorphous matrix (Fig. S9a). The corresponding TiO_2-protected Si photoanode only showed a ~70 h lifetime for PEC operation (Fig. S9b).

The critical role of water vapor exposure in the post-ALD treatment is further demonstrated by annealing the pristine TiO_2 films in an N_2 atmosphere or under $TiCl_4$ exposure instead. Annealing TiO_2 films in the N_2 atmosphere showed almost the same peak intensity in XPS Cl 2*p*, Ti 2*p* core spectrum as compared to pristine TiO_2 film (Fig. S10a, b), suggesting the inert gas atmosphere wouldn't change the chemical composition of the ALD film. Thus, the PEC performance of N_2-annealed TiO_2 film had a similar lifetime performance as pristine TiO_2 (10% decay within 29 h, Fig. S10c). Annealing Si/TiO_2 in the $TiCl_4$ atmosphere brought extra Cl impurities to the film and exhibited acute chemical instability. A large amount of corrosion spots emerged after 1 day of immersion (Fig. S11a–c). The drastic drop of peak intensity in XPS Cl 2*p*, Ti 2*p*, and O 1*s* spectra demonstrated the quick dissolution

of TiO_2 from the film (Fig. S11d–f). Correspondingly, $TiCl_4$-treated TiO_2 film showed a very short PEC protection lifetime with 10% photocurrent decay in only 1 h (Fig. S12). These control experiments also proved the critical role of Cl impurities in determining the chemical stability and protection lifetime of ALD TiO_2 films.

Besides $TiCl_4$ precursor, tetrakis(dimethylamido)titanium (TDMAT) is another typical Ti source for ALD of TiO_2 film. However, growing TiO_2 by TDMAT at the same low temperature (100 °C) would leave a substantial amount of molecular ligand residues. These big residual molecules could reduce TiO_2 film density and even result in pores formation[46,47]. Therefore, ALD of TiO_2 was conducted under the recommended temperature (T = 250 °C) using TDMAT as Ti precursor to understand the precursor relationship with the water treatment strategy and corresponding PEC performance. The as-grown TiO_2 film clearly showed an appreciable amount of nanoparticles on the surface, suggesting crystallization already occurred during the growth (Fig. S13a). However, the water treatment did not introduce an obvious change to the surface nanoparticles (Fig. S13b). From XPS spectra, a small N peak was detected from both TiO_2 films before and after water treatment, with just an infinitesimal change in its intensity (Fig. S13c). Integrating the N and Ti peak areas revealed a much smaller N:Ti ratio reduction of ~9% compared to that of Cl:Ti ratio (27%) from the $TiCl_4$ precursor. This low removal ratio of TDMAT residues could be attributed to the limited diffusion as a result of the high steric hindrance from the large dimethylamido ligands. Accordingly, the lifetime of TiO_2 films made from TDMAT was only slightly extended from ~150 to ~190 h after the water treatment (Fig. S13e), much shorter than the ~600 h offered by water-treated TiO_2 films made from $TiCl_4$. This result further evidenced that TDMAT may not be the optimal choice for ALD of protective TiO_2 films, as it introduces crystalline nanoparticles under conditions necessary to achieve sufficiently high ALD reactions. This result provided additional support to our hypothesis that crystal-free is essential to achieve a long protection lifetime, and small molecule $TiCl_4$ precursor is the optimal choice to achieve this goal.

In conclusion, we showed that post-ALD water treatment could partially remove the unreacted Cl ligands in ALD amorphous TiO_2 films without introducing additional crystallization, thereby largely improving the film's lifetime for Si-photoelectrode protection. In amorphous TiO_2 films deposited at low temperatures, residual ligands are inevitable. Their presence could significantly increase the film reactivity in alkaline electrolytes, resulting in pinhole formation and quick dissolution. Removing the residual Cl ligands by completing the reaction with extra water exposure led to the closer-to-ideal stoichiometry of TiO_2 film with improved Ti-O-Ti network continuousness. The amorphous film structure was well retained during this extended ALD process, possibly due to the limited mobility of Ti-O polyhedrons inside the amorphous matrix. When applied as a Si photoanode protection layer, this homogeneous amorphous TiO_2 film exhibited an ultra-stable protection performance in an alkaline solution, maintaining a very high saturated J_{ph} at 30 mA/cm^2 for ~600 h. This discovery provided a promising solution to decouple the crystallization from raising the ALD reaction completeness. The nearly perfect amorphous ALD film with controlled stoichiometry may enable an essential manufacturing capability leading the PEC photoelectrodes to meet the industrial standard.

Methods

ALD synthesis of TiO_2 thin films

The n-type Si wafers in our experiments were 380-μm-thick, 3-inch-diameter, single-side polished, <100> oriented, and with a resistivity of 1–10 Ω·cm. Prior to ALD, Si wafers were washed with acetone, isopropanol, and deionized (DI) water in an ultrasonic bath for 20 min sequentially, followed by immersing in 5 wt% HF solution to remove the native oxide. TiO_2 was deposited in a homemade ALD system following reported procedures[2,9]. In specific, N_2 gas with a flow rate of 40 sccm was introduced into the chamber to serve as the carrier gas. The system base pressure was kept at 780 mTorr. The chamber temperature was maintained at 100 °C for depositions. Precursors used for TiO_2 deposition were $TiCl_4$ (Sigma-Aldrich, 99.9%) and DI H_2O. $TiCl_4$ (Sigma-Aldrich, 99.9%). Both precursor vapors were pulsed into the deposition chamber separately with a pulsing time of 0.5 s each and separated by 60 s N_2 purging. Therefore, one deposition cycle involves 0.5 s of H_2O pulse + 60 s of N_2 purging + 0.5 s of $TiCl_4$ pulse + 60 s of N_2 purging. Through this procedure, ~15 nm TiO_2 film was obtained after 200 cycles. For TDMAT-TiO_2 film, the film was deposited under a recommended temperature of 250 °C in Fiji G2 ALD with TDMAT precursor (Sigma-Aldrich, 99.99%) with 300 cycles for comparison.

Post-ALD water treatment

Immediately after the normal ALD procedure being completed, additional 2400 water pulses were introduced to the ALD chamber. Each water pulse was separated by 10 s N_2 purging. The other chamber conditions remained the same. After this water treatment procedure is completed, the chamber was cooled down under N_2 flow naturally before the sample was removed.

Free-standing TiO_2 film preparation

To avoid the strong background signal from the Si wafer in STEM nano diffraction, free-standing TiO_2 films were prepared by ALD on a sacrificial PVP (polyvinylpyrrolidone) layer. 2% PVP aqueous solution was prepared and spin-coated on a Si wafer at 3000 rpm for 30 s. PVP-coated Si wafer was used in the ALD syntheses of amorphous TiO2 films under 100 °C for 200 cycles of deposition. Each cycle includes 0.5 s of H_2O pulse + 60 s of N_2 purging + 0.5 s of $TiCl_4$ pulse + 60 s of N_2 purging. Accordingly, the additional 2400 cycles of water treatment were conducted after normal growth. After synthesis, samples were immersed in water at room temperature for 2 h to release the TiO_2 film. The free-standing TiO_2 films were scooped by TEM grids for STEM characterizations.

PEC electrode preparation

Ni films were deposited on TiO_2-coated Si by sputtering using a CVC 601 DC sputtering system. The substrate was rotated at a speed of 5 rpm with argon flow at 25 sccm. The deposition was performed under 10 mTorr with 120 s deposition time. Then, the backside of the Si wafer were scratched by a diamond scribe and covered by Ga/In eutectic mixture. The silver paste was applied to fix the metal leads to the Ga/In eutectic mixture to achieve good Ohmic contact. After drying in a fume hood, the entire backside and partial front side of the Si/TiO_2/Ni electrodes were encapsulated by Epoxy (Loctite, 9460) with an exposed active area of ~0.05 cm^2. ImageJ were used to determine the exposed electrode area.

Electrochemical characterizations

The PEC tests were carried out in a typical three-electrode electrochemical setup with Si/TiO_2/Ni as the working electrode, a Pt wire as a counter electrode, and a Hg/HgO electrode as a reference electrode. The electrolyte was 1 M KOH aqueous solution. For the cyclic voltammetry (CV) and chronoamperometry measurement, working electrodes were illuminated by a 150 W Xenon lamp coupled with an AM 1.5 global filter with a light intensity of 100 mW cm^{-2} (one sun). Chronoamperometry curves were measured at a constant bias of 1.8 V vs. RHE. Electrochemical impedance spectroscopy (EIS) was conducted under open circuit voltage from 100 kHz to 0.1 Hz. All electrochemical curves were recorded using an Autolab PGSTAT302N station.

Materials characterizations

Scanning electron microscopy (SEM) images were acquired on a Zeiss LEO 1530 field-emission microscope with a gun voltage of 5 kV and a working distance of ~3.5 mm. X-ray photoelectron spectroscopy was

acquired by Thermo Scientific K-alpha XPS instrument. Atomic force microscopy (AFM) topography was obtained using an XE-70 Park System. Device corrosion area percentage were statistically analyzed by ImageJ. Four-dimensional scanning transmission electron microscopy (4D-STEM) was performed using Thermo Fisher Scientific Themis Z STEM operated at 300 kV and equipped with an electron microscopy pixel array detector (EMPAD) to acquire nano-diffraction patterns from different sampling areas within the films[48]. The intensity variance of acquired nano-diffractions was calculated[49]. EDS was performed using FEI Themis Z microscope at 300 kV equipped with four Super-X detectors, and the chemical composition of amorphous films was obtained by analyzing EDS spectra using FEI Vlox software and Kα energies for Ti, Cl, and O. The presence of crystalline phases within the amorphous matrix was investigated by observation of film using low angle annular dark field (LAADF) STEM imaging, including diffraction contrast.

Computational method

The amorphous TiO_2 structure was obtained through a melt-quenched process using the MA potential[50]. The structure was firstly melted in an NVT ensemble at 5000 K for 50 ps with a timestep of 0.5 fs, and cooled down to 3000 K with a timestep of 0.5 fs and 200 ps simulation time. Next, the model was equilibrated at 3000 K for another 50 ps. Finally, the model was annealed from 3000 K down to 300 K at a cooling step of 1 K/ps, equilibrated at 300 K for 100 ps, and statically optimized to minimal energy to obtain the final quenched atomic structure. The a-TiO_2 model consists of 87 atoms within a cubic box. The density of the structure model is consistent with the typical experimental density value of amorphous TiO_2 at room temperature ($3.84\ g/cm^3$)[51]. The electronic property of amorphous TiO_2 with and without Cl ligands was then calculated using density functional theory (DFT) implemented in the Vienna ab initio simulation (VASP) package[52,53]. The generalized gradient approximation exchange-correlation functional Perdew, Burke, and Ernzerhof (PBE)[54] with the Hubbard U correction[55,56] was applied for the structure optimization and the density of states calculation. The U value of 4.2 eV was applied to Ti atoms. The projector augmented wave method (PAW)[57] was used for the effective potential for all atoms. The PAW potentials used in these calculations have valence electron configurations of $3p^6 4s^2 3d^2$ for Ti, $2s^2 2p^4$ for O, and $3s^2 3p^5$ for Cl. The plane wave cutoff energy of 520 eV was used in all the calculations. The convergence criteria were 10^{-6} eV/cell for electronic self-consistent and 0.05 eV/Å for ionic relaxation, respectively. The Tetrahedron method with Blöchl corrections was applied for the density of states calculation.

Data availability

All data from this study are available within the Article and its Supplementary Information. The raw data used in this study are available from the corresponding author upon reasonable request.

Code availability

All processed data were available within the Article. The raw data used is available upon reasonable request.

References

1. Lewis, N. S. Research opportunities to advance solar energy utilization. *Science* **351**, aad1920 (2016).
2. Yu, Y. et al. Enhanced photoelectrochemical efficiency and stability using a conformal TiO_2 film on a black silicon photoanode. *Nat. Energy* **2**, 17045 (2017).
3. Fu, H. J. et al. Enhanced stability of silicon for photoelectrochemical water oxidation through self-healing enabled by an alkaline protective electrolyte. *Energy Environ. Sci.* **13**, 4132–4141 (2020).
4. Chen, S. & Wang, L.-W. Thermodynamic oxidation and reduction potentials of photocatalytic semiconductors in aqueous solution. *Chem. Mater.* **24**, 3659–3666 (2012).
5. Sun, K. et al. Stable solar-driven oxidation of water by semiconducting photoanodes protected by transparent catalytic nickel oxide films. *Proc. Natl Acad. Sci. USA* **112**, 3612–3617 (2015).
6. Chen, Y. W. et al. Atomic layer-deposited tunnel oxide stabilizes silicon photoanodes for water oxidation. *Nat. Mater.* **10**, 539–544 (2011).
7. George, S. M. Atomic layer deposition: an overview. *Chem. Rev.* **110**, 111–131 (2010).
8. Ros, C. et al. Insight into the degradation mechanisms of atomic layer deposited TiO_2 as photoanode protective layer. *ACS Appl. Mater. Interfaces* **11**, 29725–29735 (2019).
9. Yu, Y. et al. Metastable intermediates in amorphous titanium oxide: a hidden role leading to ultra-stable photoanode protection. *Nano Lett.* **18**, 5335–5342 (2018).
10. Cai, Q., Hong, W., Jian, C., Li, J. & Liu, W. Insulator layer engineering toward stable Si photoanode for efficient water oxidation. *ACS Catal.* **8**, 9238–9244 (2018).
11. Hu, S. et al. Amorphous TiO_2 coatings stabilize Si, GaAs, and GaP photoanodes for efficient water oxidation. *Science* **344**, 1005–1009 (2014).
12. Siddiqi, G. et al. Stable water oxidation in acid using manganese-modified TiO_2 protective coatings. *ACS Appl. Mater. Interfaces* **10**, 18805–18815 (2018).
13. Nandjou, F. & Haussener, S. Degradation in photoelectrochemical devices: review with an illustrative case study. *J. Phys. D Appl. Phys.* **50**, 124002 (2017).
14. Buabthong, P. et al. Failure modes of protection layers produced by atomic layer deposition of amorphous TiO_2 on GaAs anodes. *Energy Environ. Sci.* **13**, 4269–4279 (2020).
15. Shen, X. et al. Defect-tolerant TiO_2-coated and discretized photoanodes for> 600 h of stable photoelectrochemical water oxidation. *ACS Energy Lett.* **6**, 193–200 (2020).
16. Digdaya, I. A., Adhyaksa, G. W. P., Trześniewski, B. J., Garnett, E. C. & Smith, W. A. Interfacial engineering of metal-insulator-semiconductor junctions for efficient and stable photoelectrochemical water oxidation. *Nat. Commun.* **8**, 1–8 (2017).
17. Quinn, J., Hemmerling, J. & Linic, S. Maximizing solar water splitting performance by nanoscopic control of the charge carrier fluxes across semiconductor–electrocatalyst junctions. *ACS Catal.* **8**, 8545–8552 (2018).
18. Reed, P. J., Mehrabi, H., Schichtl, Z. G. & Coridan, R. H. Enhanced electrochemical stability of TiO_2-protected, Al-doped ZnO transparent conducting oxide synthesized by atomic layer deposition. *ACS Appl. Mater. Interfaces* **10**, 43691–43698 (2018).
19. Kavan, L., Tétreault, N., Moehl, T. & Grätzel, M. Electrochemical characterization of TiO_2 blocking layers for dye-sensitized solar cells. *J. Phys. Chem. C.* **118**, 16408–16418 (2014).
20. Lee, J. & Oh, J. Nanopixelated cuprous oxide photocathodes for durable photoelectrochemical water splitting. *ACS Energy Lett.* **7**, 3244–3250 (2022).
21. Mishra, S. et al. Structural properties of thin ZnO films deposited by ald under O-rich and Zn-rich growth conditions and their relationship with electrical parameters. *Materials* **14**, 4048 (2021).
22. Triyoso, D. et al. Impact of deposition and annealing temperature on material and electrical characteristics of ALD HfO_2. *J. Electrochem. Soc.* **151**, F220 (2004).
23. Härkönen, E. et al. $Al_xTa_yO_z$ mixture coatings prepared using atomic layer deposition for corrosion protection of steel. *Chem. Vap. Depos.* **19**, 194–203 (2013).
24. Härkönen, E. et al. Interface control of atomic layer deposited oxide coatings by filtered cathodic arc deposited sublayers for improved corrosion protection. *Mater. Chem. Phys.* **147**, 895–907 (2014).
25. Liu, R., Zheng, Z., Spurgeon, J. & Yang, X. Enhanced photoelectrochemical water-splitting performance of semiconductors by surface passivation layers. *Energy Environ. Sci.* **7**, 2504–2517 (2014).

26. Nunez, P. et al. Characterization of electronic transport through amorphous TiO_2 produced by atomic layer deposition. *J. Phys. Chem. C.* **123**, 20116–20129 (2019).
27. Saric, I. et al. Residual chlorine in TiO_2 films grown at low temperatures by plasma enhanced atomic layer deposition. *Thin Solid Films* **628**, 142–147 (2017).
28. Zhao, C. et al. Metal sputtering buffer layer for high performance Si-based water oxidation photoanode. *ACS Appl. Energy Mater.* **3**, 8216–8223 (2020).
29. Zhou, X. et al. 570 mV photovoltage, stabilized n-Si/CoOx heterojunction photoanodes fabricated using atomic layer deposition. *Energy Environ. Sci.* **9**, 892–897 (2016).
30. Moreno-Hernandez, I. A., Brunschwig, B. S. & Lewis, N. S. Tin oxide as a protective heterojunction with silicon for efficient photoelectrochemical water oxidation in strongly acidic or alkaline electrolytes. *Adv. Energy Mater.* **8**, 1801155 (2018).
31. Fu, H. J. et al. Catalytic open-circuit passivation by thin metal oxide films of p-Si anodes in aqueous alkaline electrolytes. *Energy Environ. Sci.* **15**, 334–345 (2022).
32. Das, C., Kot, M., Henkel, K. & Schmeisser, D. Engineering of sub-nanometer SiO_x thickness in Si photocathodes for optimized open circuit potential. *ChemSusChem* **9**, 2332–2336 (2016).
33. Bressers, P., Kelly, J., Gardeniers, J. G. & Elwenspoek, M. Surface morphology of p-type (100) silicon etched in aqueous alkaline solution. *J. Electrochem. Soc.* **143**, 1744 (1996).
34. Moitzheim, S. et al. Chlorine doping of amorphous TiO_2 for increased capacity and faster Li^+-ion storage. *Chem. Mater.* **29**, 10007–10018 (2017).
35. ABIDIN, Z., MATSUE, N. & HENMI, T. Dissolution mechanism of nano-ball allophane with dilute alkali solution. *Clay Sci.* **12**, 213–222 (2004).
36. Kubicki, J., Xiao, Y. & Lasaga, A. Theoretical reaction pathways for the formation of $[Si(OH)_5]^{1-}$ and the deprotonation of orthosilicic acid in basic solution. *Geochim. Cosmochim. Acta* **57**, 3847–3853 (1993).
37. Heard, C. J. et al. Zeolite (in) stability under aqueous or steaming conditions. *Adv. Mater.* **32**, 2003264 (2020).
38. Kubala, N. G., Rowlette, P. C. & Wolden, C. A. Plasma-enhanced atomic layer deposition of anatase TiO_2 using $TiCl_4$. *J. Phys. Chem. C.* **113**, 16307–16310 (2009).
39. Hwang, J. et al. Nanoscale structure and structural relaxation in $Zr_{50}Cu_{45}Al_5$ bulk metallic glass. *Phys. Rev. Lett.* **108**, 195505 (2012).
40. Luo, Z. et al. Multifunctional nickel film protected n-type silicon photoanode with high photovoltage for efficient and stable oxygen evolution reaction. *Small Methods* **3**, 1900212 (2019).
41. Mackus, A. J., Verheijen, M. A., Leick, N., Bol, A. A. & Kessels, W. M. Influence of oxygen exposure on the nucleation of platinum atomic layer deposition: consequences for film growth, nanopatterning, and nanoparticle synthesis. *Chem. Mater.* **25**, 1905–1911 (2013).
42. Mattinen, M. et al. Atomic layer deposition of crystalline molybdenum oxide thin films and phase control by post-deposition annealing. *Mater. Today Chem.* **9**, 17–27 (2018).
43. Aarik, J., Aidla, A., Mändar, H. & Sammelselg, V. Anomalous effect of temperature on atomic layer deposition of titanium dioxide. *J. Cryst. Growth* **220**, 531–537 (2000).
44. Shi, J. et al. Electron microscopy observation of TiO_2 nanocrystal evolution in high-temperature atomic layer deposition. *Nano Lett.* **13**, 5727–5734 (2013).
45. Chiappim, W. et al. Relationships among growth mechanism, structure and morphology of PEALD TiO_2 films: the influence of O_2 plasma power, precursor chemistry and plasma exposure mode. *Nanotechnology* **27**, 305701 (2016).
46. Dufond, M. E. et al. Quantifying the extent of ligand incorporation and the effect on properties of TiO_2 thin films grown by atomic layer deposition using an alkoxide or an alkylamide. *Chem. Mater.* **32**, 1393–1407 (2020).
47. Sinha, A. et al. Area selective atomic layer deposition of titanium dioxide: effect of precursor chemistry. *J. Vac. Sci. Technol. B Microelectron. Nanometer. Struct. Process. Meas. Phenom.* **24**, 2523–2532 (2006).
48. Im, S. et al. Medium-range ordering, structural heterogeneity, and their influence on properties of Zr-Cu-Co-Al metallic glasses. *Phys. Rev. Mater.* **5**, 115604 (2021).
49. Im, S. et al. Direct determination of structural heterogeneity in metallic glasses using four-dimensional scanning transmission electron microscopy. *Ultramicroscopy* **195**, 189–193 (2018).
50. Matsui, M. & Akaogi, M. Molecular dynamics simulation of the structural and physical properties of the four polymorphs of TiO_2. *Mol. Simul.* **6**, 239–244 (1991).
51. Saleem, M. R., Honkanen, S. & Turunen, J. In *IOP Conference Series: Materials Science and Engineering* 012008 (IOP Publishing, 2013).
52. Kresse, G. & Furthmüller, J. Efficient iterative schemes for ab initio total-energy calculations using a plane-wave basis set. *Phys. Rev. B* **54**, 11169 (1996).
53. Kresse, G. & Furthmüller, J. Efficiency of ab-initio total energy calculations for metals and semiconductors using a plane-wave basis set. *Comput. Mater. Sci.* **6**, 15–50 (1996).
54. Perdew, J. P., Burke, K. & Ernzerhof, M. Generalized gradient approximation made simple. *Phys. Rev. Lett.* **77**, 3865 (1996).
55. Hubbard, J. Electron correlations in narrow energy bands. *Proc. R. Soc. A Math. Phys. Eng. Sci.* **276**, 238–257 (1963).
56. Anisimov, V. I., Zaanen, J. & Andersen, O. K. Band theory and Mott insulators: Hubbard U instead of Stoner I. *Phys. Rev. B* **44**, 943 (1991).
57. Kresse, G. & Joubert, D. From ultrasoft pseudopotentials to the projector augmented-wave method. *Phys. Rev. B* **59**, 1758 (1999).

Acknowledgements

Research primarily supported by the US Department of Energy (DOE), Office of Science, Basic Energy Sciences (BES), under Award # DE-SC0020283.

Author contributions

Y.D. and X.W. conceived the ideas and designed the experiments. X.W., D.M., and J.H. supervised the research. Y.D. and L.G. conducted ALD growth and device fabrication. Y.D. performed SEM, XPS, and electrochemical characterizations. M.A. carried out STEM and EDS mapping. J.M. conducted DFT calculations. C.C. performed AFM topography scanning. J.L. conducted Ni sputtering. Y.D. and Z.Z. performed XPS analysis. Y.D. and X.W. analyzed the data and wrote the manuscript. All authors discussed the experiment and contributed to the manuscript preparation.

Competing interests

The authors declare no competing interest.

Additional information

Supplementary information The online version contains supplementary material available at https://doi.org/10.1038/s41467-023-37154-z.

Correspondence and requests for materials should be addressed to Xudong Wang.

Peer review information *Nature Communications* thanks the anonymous reviewers for their contribution to the peer review of this work. Peer reviewer reports are available.

Reprints and permissions information is available at http://www.nature.com/reprints

Publisher's note Springer Nature remains neutral with regard to jurisdictional claims in published maps and institutional affiliations.

https://doi.org/10.1038/s41467-023-37154-z

Open Access This article is licensed under a Creative Commons Attribution 4.0 International License, which permits use, sharing, adaptation, distribution and reproduction in any medium or format, as long as you give appropriate credit to the original author(s) and the source, provide a link to the Creative Commons license, and indicate if changes were made. The images or other third party material in this article are included in the article's Creative Commons license, unless indicated otherwise in a credit line to the material. If material is not included in the article's Creative Commons license and your intended use is not permitted by statutory regulation or exceeds the permitted use, you will need to obtain permission directly from the copyright holder. To view a copy of this license, visit http://creativecommons.org/licenses/by/4.0/.

© The Author(s) 2023